Analyzing the identification mechanism of graphite and clay minerals in coal and gangue using X-rays

Jianqiang Yin [1], Hongzheng Zhu [1, 2], Jinbo Zhu [1], Qiuyu Zeng [1], Liansheng Li [1], Chenguang Yang [3]

[1] School of Materials Science and Engineering, Anhui University of Science and Technology, 232001 Huainan, China

[2] State Key Laboratory of Ming Response and Disaster Prevention and Control in Deep Coal Mines, Anhui University of Science and Technology, 232001 Huainan, China

[3] School of Mechanical and Automotive Engineering, Anhui Wenda University of Information Engineering, 231201 Hefei, China

Corresponding authors: hzzhu@aust.edu.cn (H. Zhu), pgb2@aust.edu.cn (J. Zhu)

Abstract: Three types of chelating depressants were studied for chalcopyrite/pyrite separation, including S-S, S-O, and O-O types, via density functional theory calculations and microflotation. The calculation results indicate that the depressant's chelating atoms have large coefficient and great activity according to the molecular frontier orbital (HOMO and LUMO) and the orbital coefficients. For S-S type of depressant, S atom in both keto or enol forms won't affect their HOMO and LUMO patterns and the orbital contributions. For S-O type, the presence of N atom in the ring structure of a molecular will increase the reactivity of O-Cu while weak S-Cu. For O-O type, the electron supply capacity of benzene ring is higher than strain chain, and atom N in strain chain increased their electron supply capacity. The microflotation results basically confirmed the prediction based on the calculation. The simulation results demonstrate that the interaction of a depressant with metals and minerals are affected obviously by the spatial structure and electronic structure of an atom in its molecular.

Keywords: X-rays, coal gangue identification, photoelectric separation, grayscale model, pixel volume

1. Introduction

In China, coal is still the most important fossil energy resource and is far more abundant than oil and natural gas (Wang et al., 2019). In coal mining, gangue as the primary solid waste mixed with coal contributes to a reduction in the efficiency of coal production (Wang et al., 2019), thus an efficient separation of coal from gangue is necessary for the clean utilization of coal (O'Keefe et al., 2013; Wu and Chen, 2018); Traditional methods of coal/gangue separation include manual separation, wet separation, and dry separation (Jia et al., 2017; Li, H.L. et al., 2021); Manual separation is not only costly but also severely restricts the efficiency of mineral processing and could adversely affect workers' health (Lv et al., 2020; O'Connor); Wet separation must be carried out in liquid; however, gangue loosens and softens in liquid (Xia et al., 2020; Zhang, M.Q. et al., 2019), leading to numerous problems such as separation difficulty (Altun et al., 2021; Zhang et al., 2021); , an increase in separation cost (Yue et al., 2021; Zhu et al., 2020); . Photoelectric separation does not involve water consumption (Chen et al., 2012); moreover, it could also help improve separation efficiency (Liu et al., 2017) and reduce costs by considering dry coal cleaning (Hu et al., 2020; Sun et al., 2015).

In 1905, Austria studied the separation of various materials by considering differences in the surface color of materials; this method was successfully applied to the separation of food and crops. It was not until the 1960s that photoelectric separation was applied in the field of mineral processing. In recent years, the photoelectric separation of coal/gangue has garnered increased attention in research/academics (Bai et al., 2021; Altman and Aaron, 2012).Wang et al. (2017) According to the

principle of three-dimensional laser scanning, a new method for separating coal from gangue based on density was proposed by, and considering this, a mathematical model suitable for coal gangue recognition was established, and the algorithms of recognition threshold and recognition rate were given. Liu et al (2018) proposed the multifractal detrended fluctuation analysis (MFDFA) method to extract the geometric features of coal gangue; moreover, the modified local singular spectrum width Δh of the contour curve sequence was extracted as the characteristic variable of coal gangue for pattern recognition. The results demonstrated that the introduction of geometric features could help improve the recognition rate of coal gangue images. Based on the coal gangue separation system that considered the differences in the surface texture and grayscale features of coal and gangue, Hou (2019) proposed a coal gangue recognition method containing gray information statistical features (GLI), gray co-occurrence matrix (GLCM) and visual features. Eshaq et al. (2020) proposed a method for distinguishing coal from gangue by using thermal energy and infrared radiation of objects; moreover, a high classification accuracy (97.83%) was obtained by this method. Dou et al. (2020) employed the relief-SVM method to find optimal features and develop the best classifiers; moreover, it was validated through the experiments considering two mining areas, wherein the mean accuracy was 95.5-97.0% and 94.0-98.0%, respectively. Guo et al. (2021) proposed a recognition method by considering the differences in the dielectric properties of coal gangue and combined it with a support vector machine (SVM); moreover, the results were accurate, and the method was efficient.

In recent years, research on the photoelectric separation of coal gangue primarily reflects the extraction of coal gangue surface texture features and the selection of algorithms (Haghighi et al., 2011). However, the nature of coal and gangue are complex (Duan et al., 2021; Yang et al., 2015); moreover, the mechanism of X-ray imaging of coal and gangue at a molecular or atomic level has not been thoroughly studied (Li, M. et al., 2021).

Thus, the differences in mineral composition between coal and gangue at a molecular/atomic level were studied here. The relationship between the grayscale and the mineral composition at molecular/atomic levels of single minerals in coal and gangue mineral components was investigated under X-ray imaging. Finally, the relationship between the mineral composition and the grayscale after each single mineral was stacked and studied; thus, a mathematical model between grayscale and mineral composition was established (He et al., 2019).

2. Experimental procedure

2.1. Materials

Carbon is the main element of coal (Jia et al., 2014), while quartz, montmorillonite, and kaolinite are widely recognized as the main components of gangue (Yuce, 2017; Zhao et al., 2018). Here, graphite was used to represent carbon. The samples used here including graphite, quartz, montmorillonite, and kaolinite were all obtained from Shanghai Aladdin Biochemical Technology (China) (Chen et al., 2018). The purity grade of these samples was 99.8% and the water content was below 0.01%. Table 1 provides details of these samples.

Table 1. Properties of samples

Sample	Particle size (μm)	Crystal formula	Molecular weight (g/mol)
Graphite	13	C	12
Quartz	65	SiO_2	60
Montmorillonite	39	$(Na,Ca)_{0.33}(Al,Mg)_2[Si_4O_{10}](OH)_2 \cdot nH_2O$	682
Kaolinite	39	$Al_2O_3 \cdot 2SiO_2 \cdot 2H_2O$	258

2.2. System

Fig. 1 shows the experimental system, consisting of four components: (1) electron beam and metal target for generating X-rays, i.e., the process of X-ray occurrence (Kalha et al., 2021); (2) a belt for placing samples; (3) an array receiver for receiving the attenuated X-rays (Gades et al., 2017); and (4) a computer for visualizing the signal (Schmidt and Flohr, 2020).
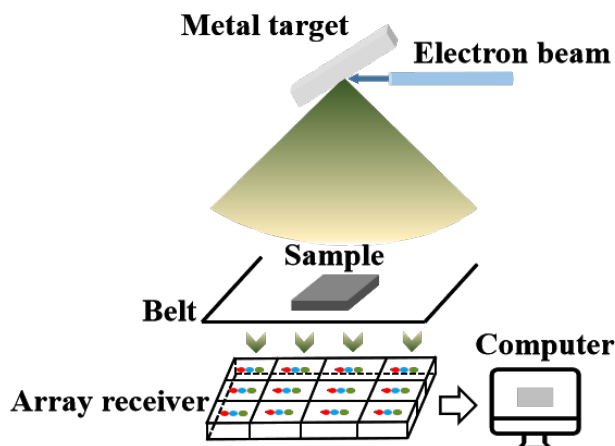
Fig. 1. Schematic of the experimental system

2.3. Measurements

The powder of each mineral was pressed into eight individual lumpish samples, the thicknesses of which were set from 7 mm to 14 mm with a gradient of 1 mm. To avoid the impact of density on the gray value, the density of all samples was maintained at 1.4243 g/cm³, i.e., the weight of the powder for thicknesses from 7 mm to 14 mm was 15.95, 18.23, 20.51, 22.79, 25.07, 27.35, 29.63, and 31.90 g, respectively. Free software Image J was used to extract the gray value of the sample image. Here, the gray value refers to the brightness level of the image from 0 to 255 that white is 255 and black is 0.

Here, the attenuation of the X-rays of the single mineral sample having a thickness of 7-21 mm was measured, where a thickness of 15-21 mm included a combination of 7 mm and other thicknesses. For exploring the attenuation of the X-rays of coal and gangue, the gray value of mineral couples with thicknesses of 15-21 mm was also measured, wherein the thickness of one mineral sample was maintained constantly at 7 mm while that of the other varied from 8 mm to 14 mm. Each test was conducted thrice and the average value was recorded as the final figure. During this process, the effect of the stacking order of the lumpish samples on the gray value was noteworthy. Hence, the gray value of sample couples was measured as shown in Fig. 2, i.e., (7 mm quartz + 9 mm graphite), (9 mm graphite + 7 mm quartz), (8 mm quartz + 9 mm graphite), and (9 mm graphite + 8 mm quartz).

As observed, the same sample couple presented the same gray value independent of the stacking order, suggesting that the stacking order could be ignored in subsequent experiments.
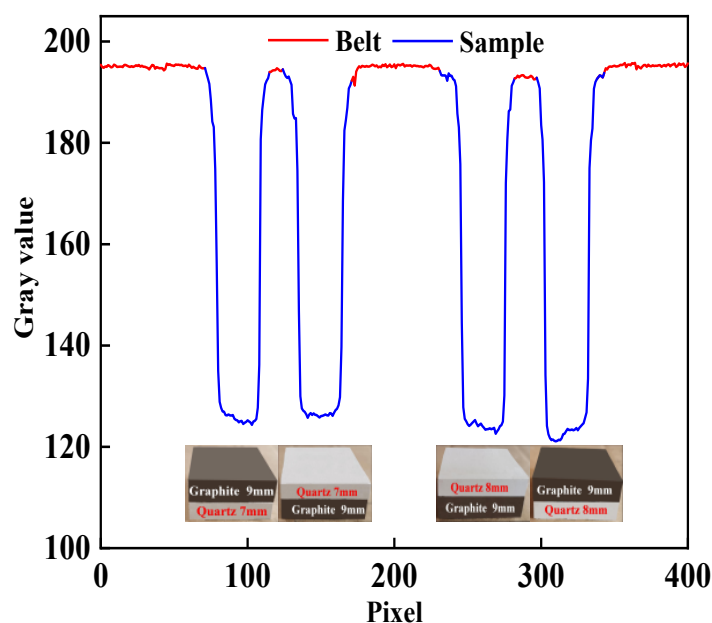
Fig. 2. The relationship between stack order and gray value

2.4. Theory and calculation

The photoelectric effect (Klassen, 2015) and Compton effect (Hajima et al., 2014) between photons and electrons are recognized to be the essential factors for the attenuation of the X-rays penetrating materials as shown in Fig. 3 (Jacquet and Bruni, 2017).
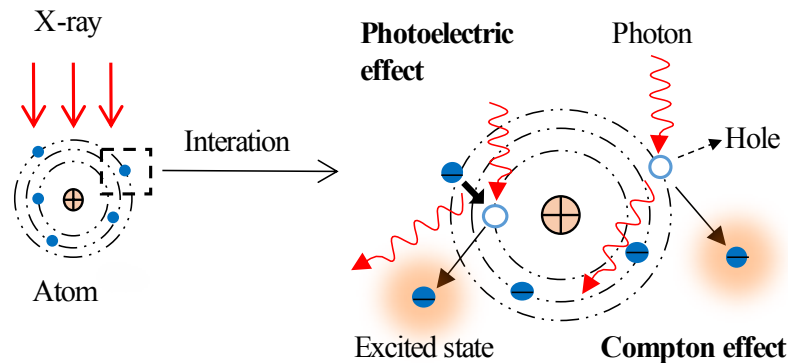
Fig. 3. Interaction between photons and electrons

However, the number of electrons being passed through by a beam of photons cannot be calculated in minerals (Bartschat et al., 2020) as photons have no volume. Hence, data considering the volume is required. In the extracted images, pixels have a relative area, while the gray value corresponding to a pixel represents the energy of the X-rays after passing through a mineral in this area. Thus, the volume was obtained and the number of electrons per unit pixel volume (N_{e-p}) was calculated (Zhang, Y.L. et al., 2019). A schematic of the calculation is graphically shown in Fig. 4.
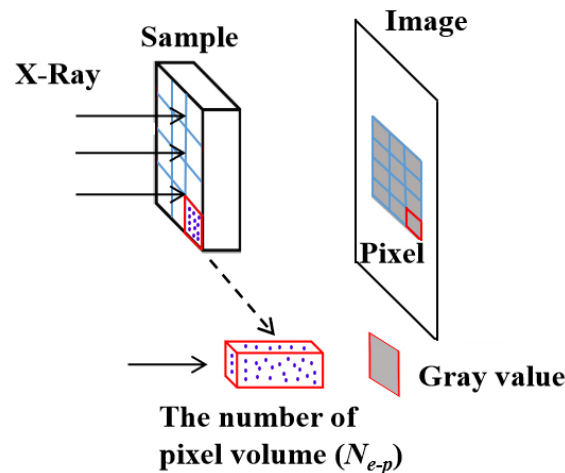
Fig. 4. Schematic for calculating the number of electrons in a pixel

The number of electrons per unit pixel volume (N_{e-p}) was calculated as per Eq. (1).

$$N_{e-p} = \frac{\frac{m}{M} \times N_A \times N_e}{\frac{S}{S_0} \times \alpha} \tag{1}$$

where m is the sample mass, N_A is the Avogadro constant, N_e is the number of extranuclear electrons of each element, S_0 is the area of the image, M is the molecular weight, S is the area covered by the mineral in the image, and a is the number of pixels in the image.

3. Results and discussion

3.1. Gray values of a single mineral and mineral couples with varying thicknesses

The attenuation of X-rays caused by different mineral samples with varying thicknesses is shown in Fig. 5, where the error is insignificant to be displayed.
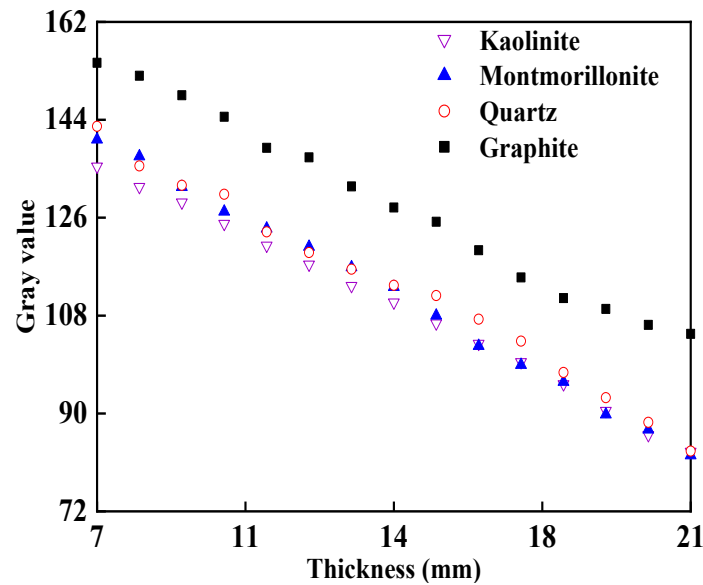
Fig. 5. X-ray attenuation of different mineral samples having varying thicknesses

It was observed that the gray value increased as the sample thickness increased; furthermore, the attenuation approximately followed the order: Kaolinite > Montmorillonite > Quartz > Graphite. Four fitting models, i.e., line, parabola, cubic, and exponent were used to fit these data, as given in Table 2.

Table 2. Fitting model considering gray value and thickness

Materials	Type	Fitting equation	R^2
Graphite	Line	$G_G = 181.746 - 3.80636\,T_G$	0.99431
	Parabola	$G_G = 187.60535 - 4.73215\,T_G + 0.03306\,T_G^2$	0.99542
	Cubic	$G_G = 156.85987 + 2.75935\,T_G - 0.53724\,T_G^2 + 0.01351\,T_G^3$	0.99798
	Exponent	$G_G = 292.93912\,e^{\frac{-T_G}{61.34561}} - 105.28747$	0.99535
Quartz	Line	$G_Q = 169.03693 + 3.9892\,T_Q$	0.99488
	Parabola	$G_Q = 163.82787 - 3.16672\,T_Q - 0.02937\,T_Q^2$	0.99300
	Cubic	$G_Q = 203.06606 - 12.76633\,T_Q + 0.69458\,T_Q^2 - 0.01724\,T_Q^3$	0.99679
	Exponent	$G_Q = 389.57474\,e^{\frac{T_Q}{98.95263}} + 418.10987$	0.99221
Montmorillonite	Line	$G_M = 169.83398 - 4.15272\,T_M$	0.99798
	Parabola	$G_M = 167.1143 - 3.72329\,T_M - 0.01534\,T_M^2$	0.99625
	Cubic	$G_M = 167.07296 - 3.71322\,T_M - 0.161\,T_M^2 + 1.81624 \times 10^{-5}\,T_M^3$	0.99801
	Exponent	$G_K = 674.26784\,e^{\frac{T_M}{-507.04839}} - 135.43814$	0.99718
Kaolinite	Line	$G_K = 162.31574 - 3.75273\,T_K$	0.99868
	Parabola	$G_K = 157.66164 - 3.01791\,T_K - 0.02624\,T_K^2$	0.99940
	Cubic	$G_K = 162.86823 - 4.2864\,T_K + 0.6982\,T_K^2 - 0.00229\,T_K^3$	0.99947
	Exponent	$G_K = 217.46162\,e^{\frac{T_K}{-70.7136}} + 375.354$	0.99941

where G_G is the gray value of graphite, G_Q is the gray value of quartz, G_M is the gray value of montmorillonite, G_K is the gray value of kaolinite, T_G is the thickness of graphite, T_Q is the thickness of quartz, T_M is thickness of montmorillonite, and T_K is the thickness of kaolinite.

As observed, the cubic model presented the highest correlation coefficient (R^2) for every mineral; hence, this model could be used to describe the gray value. The gray values of mineral couples having different thicknesses are given in Fig. 6.

The gray value of mineral couples was observed to increase with increased thickness, which was the same as that of a single mineral sample. This indicated that the attenuation of the X-rays evidently increased as the thickness of the matter to be penetrated increased.
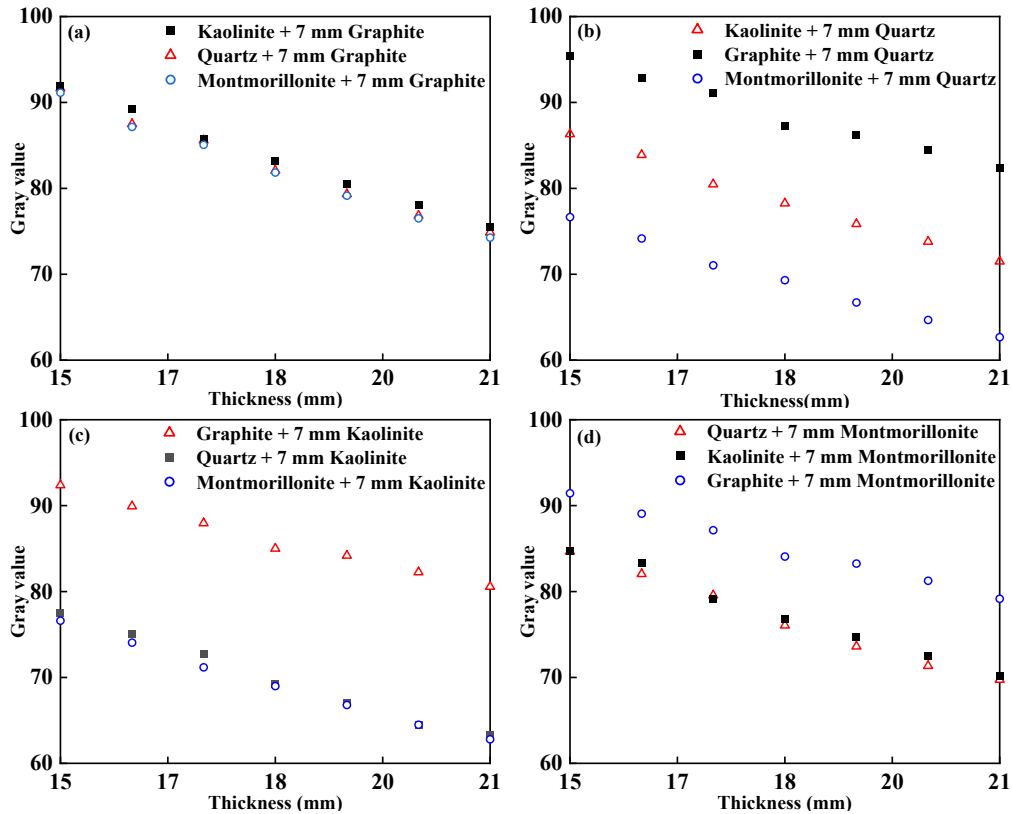
Fig. 6. Gray values of mineral couples having varying thicknesses

3.2. Relationship between gray value and electrons

Fig. 7 shows the relationship between the attenuation in gray value and the number of electrons of a single mineral. The number of electrons of quartz is considerably less than that of montmorillonite; however, the grayscale range is similar, which indicates that quartz could absorb more X-rays with fewer electrons (Lu et al., 2018). This is because the X-ray absorption coefficient of each mineral varies (Gurler et al., 2012). Fig. 7 demonstrates that the X-ray absorption coefficient was as follows: graphite < montmorillonite < kaolinite < quartz. This result indicates that coal and gangue could be identified by X-rays.
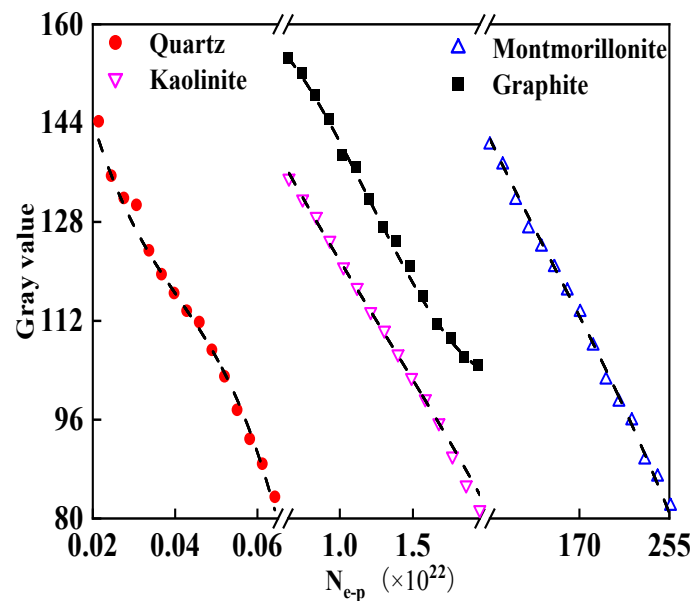
Fig. 7. Difference in gray value as a function of the number of electrons of a single mineral

Thereafter, Fig. 8 shows the relationship between the total number of electrons in mineral couples and gray value. The difference in mineral composition between coal and gangue is the difference in the carbon and quartz content (Bychev and Petrova, 2011). According to the (a) and (b) curve in Fig. 7, the difference between carbon and quartz in other minerals could be clearly observed. This is because the X-ray absorption coefficients of carbon and quartz are considerably different, which has been proved as Fig. 8.
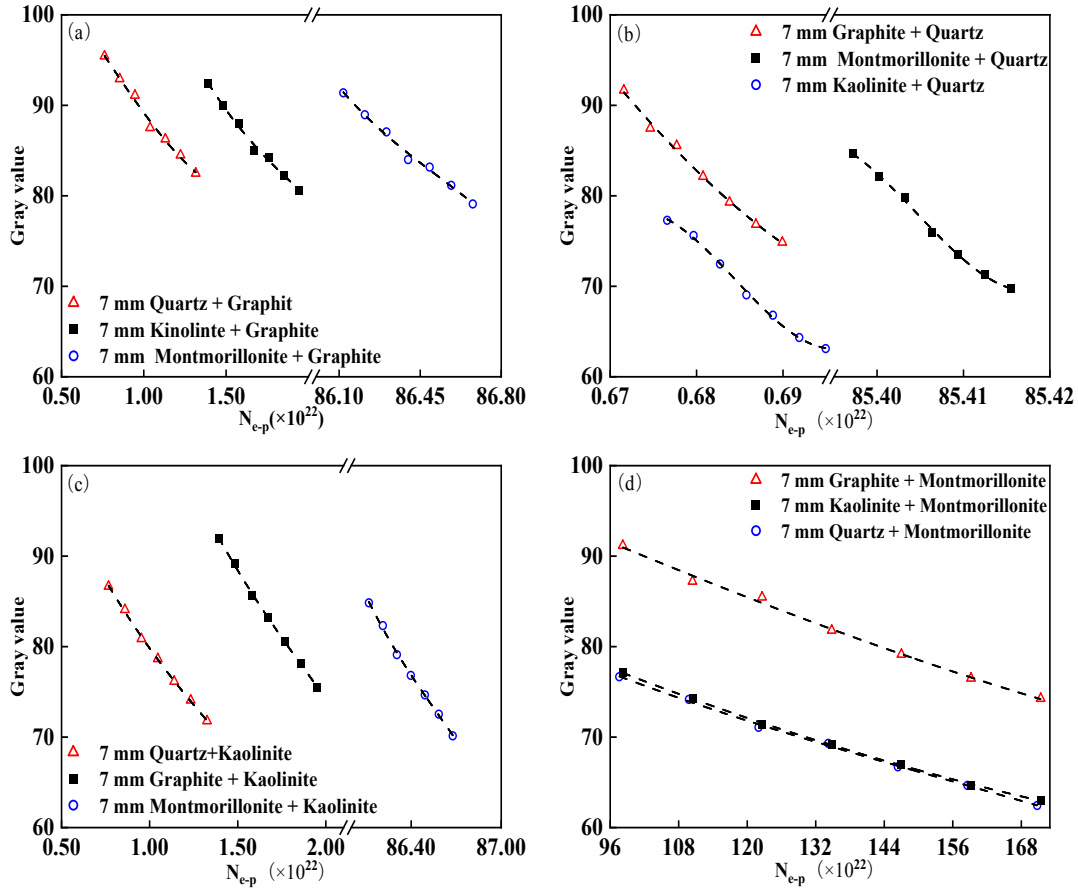
Fig. 8. Grayscale variation of mineral couples

3.3. Gray value model considering mineral couples

The relationship between the gray value of the mineral couples and that of a single mineral was then proved and established; Fig. 9 demonstrates the process.

G_S, G_C, and G' represent the gray values of a single mineral, a mineral couple, and a single mineral in a mineral couple, respectively. The grayscale model for a single mineral and that for a single mineral in a mineral couple was developed by considering the gray values of a single mineral and couple mineral, respectively; moreover, the accuracy of this model was proved by a similarity analysis by considering that $G_C = f(G_S)$ and $G' = f(G_S)$.

We considered the 7 mm quartz + (8-14 mm graphite) as an example to study and prove the accuracy of the relationship between the gray value of the mineral couples and that of the single minerals, respectively.

First, the gray value for quartz + graphite was fitted to obtain the gray equation as follows:

$$G_{G\ in\ Q} = 138.23626 + 1.18082 \times 10^{-21} N_{e-p(G+Q)} + 1.91764 \times 10^{-43} N_{e-p(G+Q)}^2 - 8.57095 \times N_{e-p(G+Q)}^3 \tag{2}$$

where $G_{G\ in\ Q}$ is the gray value considering the change of graphite in quartz, while $N_{e-p(G+Q)}$ is the sum of electrons in graphite and quartz as follows:

$$N_{e-p(G+Q)} = N_{e-p(G)} + N_{e-p(Q)} \tag{3}$$

As the thickness of quartz was constant, i.e., 7 mm, the total number of electrons in quartz was constant during the course of the experiment; hence, $N_{e-p(Q)} = 2.14 \times 10^{20}$, which was substituted into Eq. (4).

$$G'_{G\ in\ Q} = 138.24496 + 1.26172 \times 10^{-21} N_{e-p(G)} + 1.76004 \times 10^{-43} N_{e-p(G)}^{2} - -8.57095 \times 10^{-66} N_{e-p(G)}^{3} \qquad (4)$$
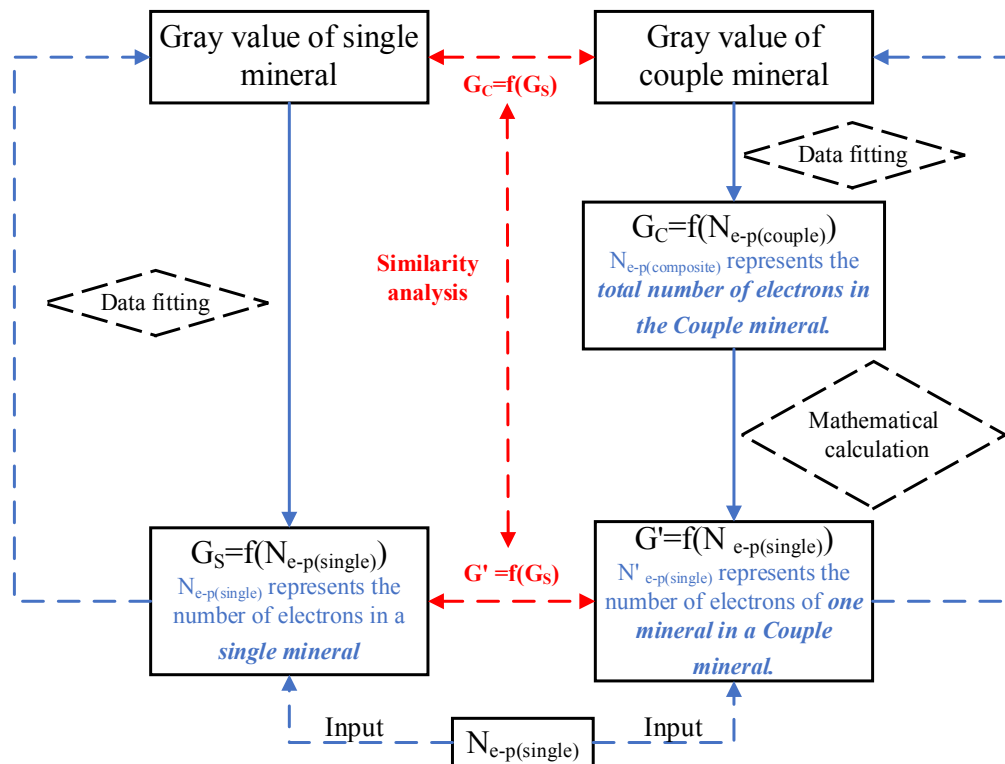
Fig. 9. Verification of the number of electrons of one mineral in a mineral couple

This equation represents the relationship between the composition of a mineral and the gray value when two kinds of minerals are mixed. For composite minerals and single minerals, there exist two equations with $N_{e-p(G)}$ as an independent variable: one considers a single quartz change; the other considers that the graphite remains unchanged, and that the quartz changes under the mixed condition of graphite and quartz.

First, to verify the relationship between the Eq. (4), the gray values of 8–14 mm quartz (G_G) and 7 mm graphite + 8–14 mm quartz ($G_{G\ in\ Q}$) considering the original data, and $G'_{G\ in\ Q}$ that was obtained by substituting N_{e-p} into Eq. (4) are shown in Table 3.

Table 3. Gray value of a single mineral and mineral couples

N_{e-p} of graphite	G_G	$G_{G\ in\ Q}$	$G'_{G\ in\ Q}$
7.40×10^{21}	133.53	91.64	90.65
8.32×10^{21}	130.96	87.54	86.75
9.24×10^{21}	130.31	85.54	84.88
1.02×10^{22}	124.39	82.15	82.02
1.11×10^{22}	121.6	79.27	79.14
1.20×10^{22}	119.52	76.85	75.32
1.29×10^{22}	117.57	74.82	74.88

The similarity analysis was undertaken by considering that $G'_{G\ in\ Q} = f(G_G)$ and $G_{G\ in\ Q} = f(G_G)$. Fig. 10 shows the changes of graphite in kaolinite, kaolinite in graphite, quartz in graphite, and graphite in quartz, respectively.

A relationship model considering other mineral couples and single minerals was deduced in the same way, as illustrated by Table 4.

The results demonstrated that the Pearson correlations between $G'_{G\ in\ Q}$ and $G_{G\ in\ Q}$ reached over 98%, indicating that the gray model for composite minerals and single minerals was more accurate; furthermore, this also proved that the gray value model considering the change of a single mineral in a mineral couple had high accuracy.

3.4. Model verification test

A gray scale model for a single mineral and mineral couple was established based on the above method. However, this was done under the condition that the N_{e-p} of a certain mineral could be quantified, which expressed the relationship between the change in the composition of a mineral and in the gray value of a mineral couple. Taking $G_{G\ in\ Q}$ as an example, theoretically, if we changed the quantity of $N_{e-p(Q)}$ the intercept of the equation would change; however, the rate of change would remain the same. Thus, we substituted $N_{e-p(Q)} = 6.42 \times 10^{20}$, 2.75×10^{20}, 2.44×10^{20}, 2.14×10^{20}, and 0 into Eq. (3), as shown in Fig. 11. G_G represents the change in gray value for a single mineral graphite. The experimental results corresponded well with theory.

Considering Fig. 11, when $N_{e-p}(Q) = 0$, the intercept of the mineral couple curve differed from that of the single mineral curve. This suggested that when the amount of content of one substance in a mineral couple became negligible, the gray value of the mineral couple differed from that of a single mineral. This is because the X-ray coefficient of mineral couples does not change immediately. Additionally, the X-ray absorption coefficient on adding quartz to graphite was smaller than that for single mineral graphite. Furthermore, the X-ray absorption coefficient on adding quartz to graphite was larger than that for single mineral graphite; moreover, this was independent of the amount of quartz added. Other minerals also conform to this rule. The results showed that the rate of change of X-ray attenuation caused by an increase in carbon content in coal and quartz content in gangue differed. Thus, the mechanism for identifying coal and gangue based on X-rays was revealed.

In this study, the gray value models of individual composition and composition couple were estab-
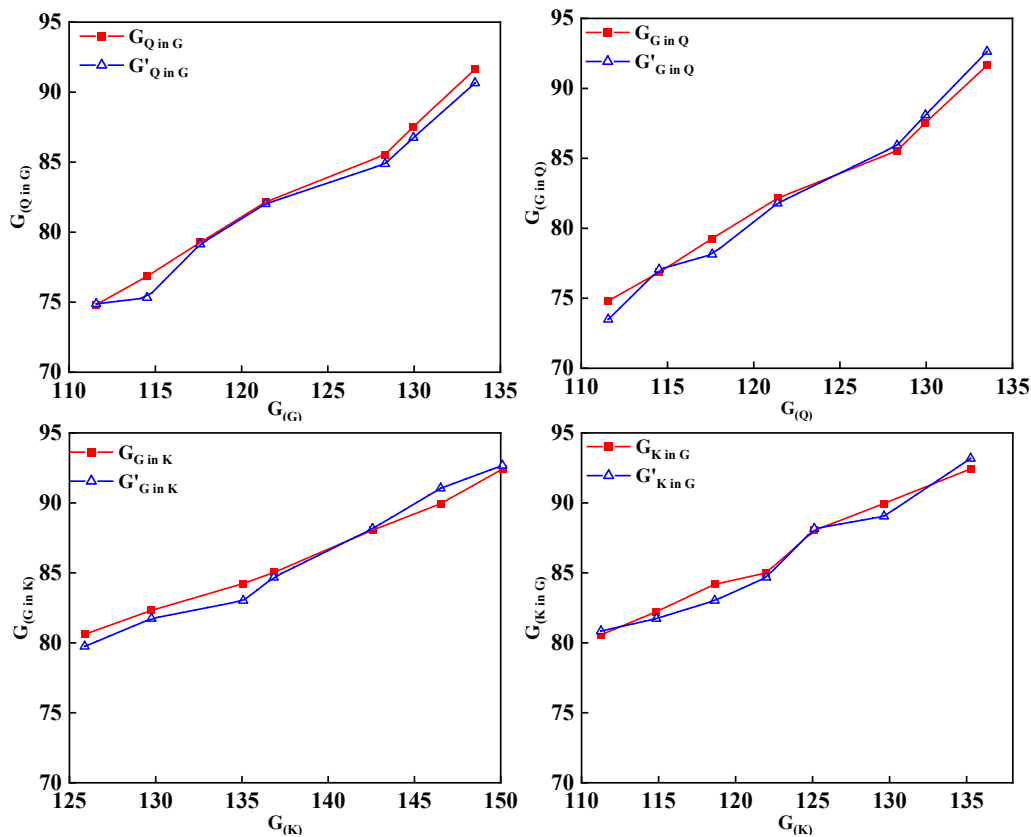
Fig. 10. Similarity analysis considering model values and measured values

lished and verified, which was meaningful for exploring the separation mechanism of coal and gangue via this invisible light technology. However, only two compositions considered in the gray value model of the mineral couple was inadequate, i.e., these models were still difficult to predict the gray value of the actual coal sample due to the complex mineral composition.

Table 4. Correlation analysis of the models

Model	Formula	Pearson correlation
$G_{K\,in\,G}$	$137.12725 + 2.36451 \times 10^{-20}\, N_{e-p(K\,in\,G)} + 4.53364 \times 10^{-42}\, N^2_{e-p(K\,in\,G)}$ $- 2.41127 \times 10^{-63}\, N^3_{e-p(K\,in\,G)}$	0.99371
$G_{G\,in\,K}$	$153.61233 - 6.45561 \times 10^{-19}\, N_{e-p(G\,in\,K)} - 2.64384 \times 10^{-40}\, N^2_{e-p(G\,in\,K)}$ $+ 8.21863 \times 10^{-60} N^3_{e-p(G\,in\,K)}$	0.99695
$G_{Q\,in\,G}$	$142.23494 - 2.91716 \times 10^{-21}\, N_{e-p(Q\,in\,G)} + 5.48491 \times 10^{-43}\, N^2_{e(Q\,in\,G)}$ $- 6.39942 \times 10^{-66}\, N^3_{e(Q\,in\,G)}$	0.99806
$G_{G\,in\,Q}$	$138.24496 + 1.26172 \times 10^{-21}\, N_{e-p(G\,in\,Q)} + 1.76004 \times 10^{43}\, N^2_{e-p(G\,in\,Q)}$ $- 8.57095 \times 10^{-66}\, N^3_{e-p(G\,in\,Q)}$	0.99685
$G_{M\,in\,G}$	$12.44658 + 9.32434 \times 10^{-23}\, N_{e-p(M\,in\,G)} - 4.57636 \times 10^{-47}\, N^2_{e-p(G\,in\,Q)}$ $+ 9.52791 \times 10^{-71}\, N^3_{e-p(G\,in\,Q)}$	0.99421
$G_{G\,in\,M}$	$-11.1246 \times 10^7 + 3.89672 \times 10^{-17}\, N_{e-p(G\,in\,M)} - 4.50066 \times 10^{-41}\, N^2_{e-p(G\,in\,M)}$ $+ 1.73282 \times 10^{-63}\, N^3_{e-p(G\,in\,M)}$	0.98546
$G_{Q\,in\,M}$	$150.78958 + 1.90946 \times 10^{-23}\, N_{e-p(Q\,in\,M)} + 6.73763 \times 10^{-48}\, N^2_{e-p(Q\,in\,M)}$ $- 3.22433 \times 10^{-72}\, N^3_{e-p(Q\,in\,M)}$	0.99648
$G_{M\,in\,Q}$	$18.9120 \times 10^{11} - 3.13056 \times 10^{-16}\, N_{e-p(M\,in\,Q)} + 3.6656 \times 10^{-36}\, N^2_{e-p(M\,in\,Q)}$ $- 1.4037 \times 10^{-60}\, N^3_{e-p(M\,in\,Q)}$	0.98845
$G_{K\,in\,M}$	$136.43112 + 5.68496 \times 10^{-23}\, N_{e-p(K\,in\,M)} - 2.46158 \times 10^{-47}\, N^2_{e-p(K\,in\,M)}$ $+ 5.1846 \times 10^{-72}\, N^3_{e-p(K\,in\,M)}$	0.99127
$G_{M\,in\,K}$	$-12.4988 \times 10^7 + 8.66875 \times 10^{-17}\, N_{e-p(M\,in\,K)} - 1.00246 \times 10^{-40}\, N^2_{e-p(M\,in\,K)}$ $+ 3.86427 \times 10^{-65}\, N^3_{e-p(M\,in\,K)}$	0.98473
$G_{K\,in\,Q}$	$171.50175 - 3.11634 \times 10^{-16}\, N_{e-p(K\,in\,Q)} + 4.5561 \times 10^{-38}\, N^2_{e-p(K\,in\,Q)}$ $- 2.21965 \times 10^{-63}\, N^3_{e-p(K\,in\,Q)}$	0.99842
$G_{Q\,in\,K}$	$128.97902 + 5.9862 \times 10^{-21}\, N_{e-p(Q\,in\,K)} - 2.334 \times 10^{-43}\, N^2_{e-p(Q\,in\,K)}$ $+ 4.66095 \times 10^{-66}\, N^3_{e-p(Q\,in\,K)}$	0.98741
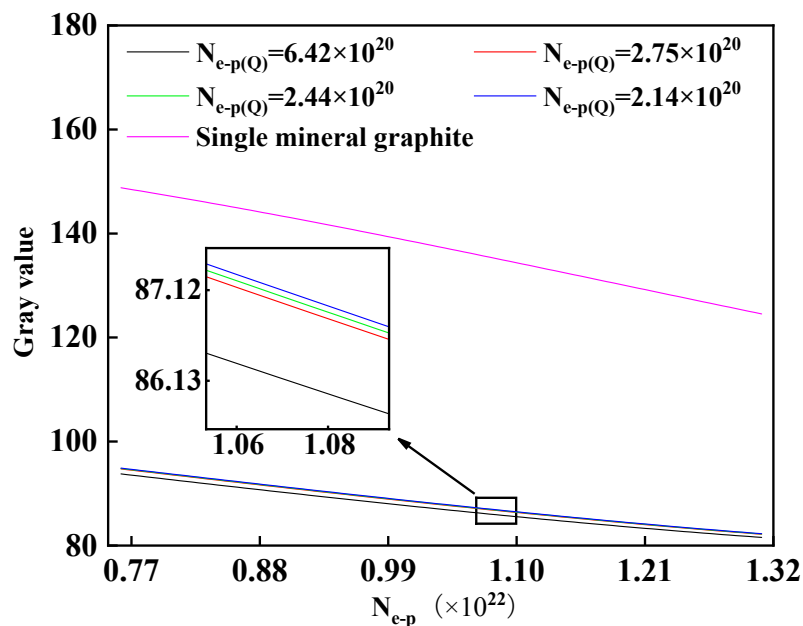
Fig. 11. Model curves for different number of electrons of quartz

4. Conclusion

Gray value is an important identification feature in the photoelectric intelligent separation of coal gangue. Studies on the mechanism for identifying coal gangue by X-rays are currently lacking; moreover, the relationship between the gray value and thickness of coal gangue cannot be used to identify coal gangue. To address this problem, a preliminary test was carried out and the following conclusions could be made:

(a) Minerals were divided according to the number of pixels in a two-dimensional image; a relationship was established between the gray value of each pixel and the number of electrons that interacted with photons; thereafter, the concept of the number of electrons per pixel volume was proposed.

(b) A model considering the gray level of a single mineral and N_{e-p} was established. Using the model, four single minerals could be accurately identified based on the given gray level.

(c) A gray scale model considering a single mineral and compound mineral was established by linking the two. After verification, it was shown that in coal and gangue, only the influence of minerals with a higher gray scale value needed consideration.

References

ALTMAN, A., AARON, R., 2012. *Dual X-ray absorptiometry*. American Journal of Physics 80(7), 621-626.

ALTUN, O., PRZIWARA, P., BREITUNG-FAES, S., KWADE, A., 2021. *Impacts of process and design conditions of dry stirred milling on the shape of product size distribution*. Minerals Engineering 163(4), 106806.

BARTSCHAT, K., BROWN, A., VAN DER HART, H.W., COLGAN, J., SCOTT, N.S., TENNYSON, J., 2020. *Computational treatment of electron and photon collisions with atoms, ions, and molecules: the legacy of Philip G Burke*. Journal of Physics B-Atomic Molecular and Optical Physics. 53(19), 192002.

BYCHEV, M.I., PETROVA, G.I., 2011. *Effect of Coal Rank on the Composition of Organic Matter (Short Communication)*. Solid Fuel Chemistry. 45(2), 95-96.

BAI, F.Y., FAN, M.Q., YANG, H.L., DONG, L.P., 2021. *Fast recognition using convolutional neural network for the coal particle density range based on images captured under multiple light sources*. International Journal of Mining Science and Technology. https://doi.org/10.1016/j.ijmst.2021.09.004

CHEN, J., CHU, K.W., ZOU, R.P., YU, A.B., VINCE, A., 2012. *Prediction of the performance of dense medium cyclones in coal preparation*. Minerals Engineering 31, 59-70.

CHEN, Y.R., XIA, W.C., XIE, G.Y., 2018. *Contact angle and induction time of air bubble on flat coal surface of different roughness*. Fuel 222, 35-41.

DOU, D.Y., ZHOU, D.Y., YANG, J.G., ZHANG, Y., 2020. *Coal and gangue recognition under four operating conditions by using image analysis and Relief-SVM*. International Journal of Coal Preparation and Utilization. 40(7), 473-482.

DUAN, C.L., YUAN, J.L., PAN, M., HUANG, T., JIANG, H.S., ZHAO, Y.M., QIAO, J.P., WANG, W.N., YU, S.J., LU, J.W., 2021. *Variable elliptical vibrating screen: Particles kinematics and industrial application*. International Journal of Mining Science and Technology. https://doi.org/10.1016/j.ijmst.2021.07.006ESHAQ, R.M.A., HU, E.Y., LI, M.G., ALFARZAEAI, M.S., 2020. *Separation Between Coal and Gangue Based on Infrared Radiation and Visual Extraction of the YCbCr Color Space*. Ieee Access 8, 55204-55220.

GADES, L.M., CECIL, T.W., DIVAN, R., SCHMIDT, D.R., ULLOM, J.N., MADDEN, T.J., YAN, D.K., MICELI, A., 2017. *Development of Thick Electroplated Bismuth Absorbers for Large Collection Area Hard X-ray Transition Edge Sensors*. Ieee Transactions on Applied Superconductivity 27(4), 1-5.

KLASSEN, S., 2011. *The Photoelectric Effect: Reconstructing the Story for the Physics Classroom*. Science & Education 20(7), 719-731.

GUO, Y.C., WANG, X.Q., WANG, S., HU, K., WANG, W.S., 2021. *Identification Method of Coal and Coal Gangue Based on Dielectric Characteristics*. Ieee Access 9, 9845-9854.

GURLER, O., OKTAR, C.H., YALCIN, S., KAYNAK, G., 2012. *Analytical formulas for calculating photoelectric attenuation coefficients*. Radiation Effects and Defects in Solids 167(12), 895-902.

HAGHIGHI, R.R., CHATTERJEE, S., VYAS, A., KUMAR, P., THULKAR, S., 2011. *X-ray attenuation coefficient of mixtures: Inputs for dual-energy CT*. Medical Physics 38(10), 5270-5279.

HAJIMA, R., HAYAKAWA, T., SHIZUMA, T., ANGELL, C.T., NAGAI, R., NISHIMORI, N., SAWAMURA, M., MATSUBA, S., KOSUGE, A., MORI, M., SEYA, M., 2014. *Application of Laser Compton Scattered gamma-ray beams to nondestructive detection and assay of nuclear material*. European Physical Journal-Special Topics 223(6), 1229-1236.

HE, J.F., ZHU, L.T., LIU, C.G., BAI, Q., 2019. *Optimization of the oil agglomeration for high-ash content coal slime based on design and analysis of response surface methodology (RSM)*. Fuel 254, 115560.

HOU, W., 2019. *Identification of Coal and Gangue by Feed-forward Neural Network Based on Data Analysis*. Journal of Coal Preparation and Utilization. 39(1), 33-43.

Hu, P., Liang, L., Xie, G., Zhou, S., Peng, Y., 2020. *Effect of slurry conditioning on flocculant-aided filtration of coal tailings studied by low-field nuclear magnetic resonance and X-ray micro-tomographyInternational*. Journal of Mining Science and Technology.30(6), 859-864.JACQUET, M., BRUNI, C., 2017. *Analytic expressions for the angular and the spectral fluxes at Compton X-ray sources*. Journal of Synchrotron Radiation 24, 312-322.

JIA, F., WANG, Q., WU, J., LI, Y., SONG, S., 2017. *Two-Dimensional Molybdenum Disulfide as a Superb Adsorbent for Removing Hg2+ from Water*. Acs Sustainable Chemistry & Engineering 5, 7410-7419.

JIA, F.F., RAMIREZ-MUNIZ, K., SONG, S.X., 2014. *Preparation and Characterization of Porous Hematite through Thermal Decomposition of a Goethite Concentrate*. Mineral Processing and Extractive Metallurgy Review 35(3), 193-201.

KALHA, C., FERNANDO, N.K., BHATT, P., JOHANSSON, F.O.L., LINDBLAD, A., RENSMO, H., MEDINA, L.Z., LINDBLAD, R., SIOL, S., JEURGENS, L.P.H., CANCELLIERI, C., ROSSNAGEL, K., MEDJANIK, K., SCHONHENSE, G., SIMON, M., GRAY, A.X., NEMSAK, S., LOEMKER, P., SCHLUETER, C., REGOUTZ, A., 2021. *Hard x-ray photoelectron spectroscopy: a snapshot of the state-of-the-art in 2020*. Journal of Physics-Condensed Matter 33(23), 233001.

LI, H.L., HAN, H., WANG, Y., DONG, X.S., YANG, H.L., FAN, M.Q., HU, Y., FENG, Z.Y., 2021. *Interaction force between coal and Na-, K- and Ca- montmorillonite 001 surfaces in aqueous solutions*. Fuel 289, 119977.

LI, M., HE, X., DUAN, Y., YANG, M., 2021. *Experimental study on the influence of external factors on image features of coal and gangue*. Journal of Coal Preparation and Utilization. 2021, 1-18.

LIU, K., ZHANG, X., CHEN, Y.Q., 2018. *Extraction of Coal and Gangue Geometric Features with Multifractal Detrending Fluctuation Analysis*. Applied Sciences-Basel 8(3), 463.

Liu, Y.Y., Lei, S.M., Huang, T., Ji, M.J., Li, Y., Fan, Y.M., 2017. *Research on mineralogy and flotation for coal-series kaolin*. Applied clay Science. 136, 37-42.

Lu, Y.J., Lin, C.N., Shan, C.X., 2018. *Optoelectronic Diamond: Growth, Properties, and Photodetection Applications*. Advanced Optical Materials. 6, 1800359.

Lv, Z., Wang, W., Xu, Z., Zhang, K., Lv, H., 2020. *Cascade network for detection of coal and gangue in the production context*. Powder Technol. 377, 361-371.

O'CONNOR, C.,2021. *Review of important developments since the 1st IMPC in 1952 in the understanding of the effects of chemical factors on flotation*. Minerals Engineering. 170, 106960.

O'KEEFE, J.M.K., BECHTEL, A., CHRISTANIS, K., DAI, S., DIMICHELE, W.A., EBLE, C.F., ESTERLE, J.S., MASTALERZ, M., RAYMOND, A.L., VALENTIM, B.V., WAGNER, N.J., WARD, C.R., HOWER, J.C., 2013. *On the fundamental difference between coal rank and coal type*. International Journal of Coal Geology 118, 58-87.

SCHMIDT, B., FLOHR, T., 2020. *Principles and applications of dual source CT*. Physica Medica-European Journal of Medical Physics 79, 36-46.

SUN, Z.M., QU, X.S., WANG, G.F., ZHENG, S.L., FROST, R.L., 2015. *Removal characteristics of ammonium nitrogen from wastewater by modified Ca-bentonites*. Applied Clay Science. 107, 46-51.

WANG, W., LI, B., YAO, X., LYU, J., NI, W., 2019. *Air pollutant control and strategy in coal-fired power industry for promotion of China's emission reduction*. Frontiers in Energy 13(2), 307-316.

WANG, W.D., ZHANG, C., 2017. *Separating coal and gangue using three-dimensional laser scanning. International*

Journal of Mineral Processing 169, 79-84.

WANG;, W., LYU;, J., LI;, Z., ZHANG;, H., YUE;, G., NI, W., 2019. *Energy conservation in China's coal-fired power industry by installing advanced units and organized phasing out backward production*. Frontiers in Energy 13(4), 798-807.

WU, X.F., CHEN, G.Q., 2018. *Coal use embodied in globalized world economy: From source to sink through supply chain*. Renewable & Sustainable Energy Reviews 81, 978-993.

XIA, Y.C., XING, Y.W., LI, M., LIU, M., TAN, J.L., CAO, Y.J., GUI, X.H., 2020. *Studying interactions between undecane and graphite surfaces by chemical force microscopy and molecular dynamics simulations*. Fuel 269, 117367.

YANG, X., FU, Z., ZHAO, J., ZHOU, E., ZHAO, Y., 2015. *Process analysis of fine coal preparation using a vibrated gas-fluidized bed*. Powder Technol. 279, 18-23.

YUCE, A.E., 2017. *Grinding Size Estimation and Beneficiation Studies Based on Simple Properties of ore Components*. Physicochemical Problems of Mineral Processing 53(1), 541-552.

YUE, G., LYU, J., LI, S., 2021. *Clean and highly-efficient utilization of coal*. Frontiers in Energy 15(1), 1-3.

ZHANG, M.Q., YU, W., CAO, Y.J., XU, H.Y., 2019. *Effect of swelling clay dispersion type on fine coal flotation*. Physicochemical Problems of Mineral Processing 55(2), 380-388.

ZHANG, Y., ZHU, H.Z., ZHU, J.B., YANG, F., HE, H., QIN, Z.Q., SHI, Q.H., PAN, G.C., 2021. *Experimental and emulational study on the role of ion in coal adsorbing kerosene: Water–kerosene interface and catenoid characteristics*. Fuel 294, 120540.

ZHANG, Y.L., MOSTAGHIMI, P., ARMSTRONG, R.T., 2019. *On the challenges of greyscale-based quantifications using X-ray computed microtomography*. Journal of Microscopy. 275(2), 82-96.

ZHAO, Y.L., CHEN, L.C., YI, H., ZHANG, Y.M., SONG, S.X., BAO, S.X., 2018. *Vanadium Transitions during Roasting-Leaching Process of Vanadium Extraction from Stone Coal*. Minerals 8(2), 63.

ZHU, H.Z., ZHU, J.B., LOPEZ VALDIVIESO, A., MIN, F.F., SONG, S.X., WANG, H., 2020. *Effect of frother addition mode on gas dispersion and coal flotation in a downflow flotation column*. Fuel 273, 117715.